

## Influence of raw material on the morphology and photocatalytic properties of graphene oxide

E.A. Huitrón-Segovia<sup>a</sup>, D. Torres-Torres<sup>a</sup>, A. Moreno-Bárcenas<sup>a</sup>, J.E. Samaniego-Benítez<sup>b</sup>, J. Ramírez-Aparicio<sup>c</sup>, A. Mantilla<sup>d</sup>, A. García-García<sup>a,\*</sup>

<sup>a</sup> Centro de Investigación en Materiales Avanzados, S.C. (CIMAV), Grupo de síntesis y modificación de nanoestructuras y materiales 2D and Laboratorio de análisis de integridad de desempeño mecánico de dispositivos y materiales avanzados, Subsede Monterrey, Av. Alianza Norte 202, Parque PIIT, Apodaca, Nuevo León 66628, Mexico

<sup>b</sup> CONAHCYT- Instituto Politécnico Nacional-Centro de Investigación en Ciencia Aplicada y Tecnología Avanzada Unidad Legaria, Calzada Legaria 694, Col. Irrigación, Ciudad de México 11500, Mexico

<sup>c</sup> CONAHCYT -Centro de Investigación en Ingeniería y Ciencias Aplicadas, Universidad Autónoma del Estado de Morelos, Av. Universidad 1001, Col. Chamilpa, Cuernavaca, Morelos 62209, Mexico

<sup>d</sup> Instituto Politécnico Nacional, Laboratorio de Fotocatálisis, CICATA-Legaria, Legaria 694, Col Irrigación, Ciudad de México 11500, Mexico

### ARTICLE INFO

#### Keywords:

Graphite  
Graphene oxide  
Photocatalysis  
Hydrogen production

### ABSTRACT

This study investigates how different types of graphite used as raw material impact graphene oxide's morphology and photocatalytic properties (GO). The research focuses on four graphite samples with distinct mesh sizes synthesized into GO using a modified Hummers method. The GO materials were characterized using X-ray diffraction (XRD), scanning electron microscopy (SEM), Fourier transform infrared spectroscopy (FTIR), UV-Vis spectroscopy, and X-ray photoelectron spectroscopy (XPS).

Key findings indicate that the source of graphite significantly influences the degree of oxidation, layer number, and interlayer spacing in the resulting GO. GO derived from graphite with a Taylor 28 mesh size exhibited an interlayer spacing of 8.47 Å, a higher content of carbonyl groups (C=O), and the highest hydrogen production rate of 1570 µmol/g over 4 h under UV irradiation. These results underscore the importance of selecting the appropriate graphite precursor to optimize GO's properties for photocatalytic applications, providing significant insights into enhancing hydrogen production efficiency through sustainable energy technologies.

### 1. Introduction

Graphene is one of the most revolutionary materials of recent times. Its isolation in 2004, as reported by A. Geim and K.S. Novoselov, marked a pivotal moment in the fields of nanotechnology and materials science [1–3]. Graphene and graphene oxide (GO) have significant potential in numerous research fields. It consists of a single or few layers of graphene sheets functionalized with oxygen-containing groups such as hydroxyl (-OH), epoxy (—O—), carbonyl (-C=O), and carboxyl (-COOH) [4]. GO is as versatile as graphene, with applications spanning electronics, solar cells, electrodes, water treatment, medical fields, reinforcement materials, and more [5,6]. Recently, significant efforts have been devoted to synthesizing GO through various methods. The most common approach involves the chemical exfoliation of graphite, with the Hummers method and its adaptations, developed over the years, being the most widely

used [7,8]. Chemically exfoliated GO retains its lamellar structure, though it exhibits lattice distortions caused by functional groups such as hydroxyl, carbonyl, and epoxy groups. [9]. The presence of these functional groups enables the separation of GO from bulk graphene into individual layers. These groups create a hydrophilic surface that facilitates the dispersion of GO in aqueous solutions and organic compounds. Additionally, it has been reported that the functional groups in GO serve as anchor points on polymeric or ceramic substrates, supporting the growth and dispersion of nanoparticles [10].

Mahmoud et al. demonstrated that the choice of graphite source is crucial in determining the oxidation degree of the resulting GO. The oxidized carbon material from natural graphite powder exhibited lower oxidation than graphite platelets and synthetic graphite powder. [11]. Another significant contribution in this field is the work by Boots et al., which highlighted the importance of the crystallinity of the starting

\* Corresponding author.

E-mail address: alejandra.garcia@cimav.edu.mx (A. García-García).

graphite. They demonstrated that graphite with higher crystallinity produces GO sheets with surface areas 19 times larger than those derived from lower-crystallinity graphite. Additionally, GO synthesized from less crystalline graphite contained more hydroxyl and carboxyl groups. In contrast, GO from more crystalline graphite predominantly featured epoxy groups on the basal plane, reflecting distinct chemical behaviors. [12]. Wu et al. also reported that the source of graphite significantly affects the number of layers in the resulting graphene oxide when using the Hummers method. Specifically, a smaller lateral size and lower crystallinity of the starting graphite result in fewer layers [13]. Therefore, chemical exfoliation is a viable alternative for large-scale graphene oxide production. However, the resulting material's quality, structure, and properties depend on the oxidation conditions process and the source or type of graphite used [14].

The search for renewable and sustainable energy sources has become critically important in recent decades due to the need to reduce reliance on fossil fuels and mitigate climate change effects. In this context, hydrogen production through photocatalytic processes is one of the most promising emerging technologies for generating clean and abundant energy. Hydrogen, as an energy carrier, offers high efficiency, produces only water as a byproduct, and can be easily stored and transported. However, a significant challenge remains in enhancing the efficiency of photocatalysts to make hydrogen production economically viable. Graphene and graphene oxide have been used for several years as photocatalytic support for different semiconductor materials in the hydrogen production reaction [15,16]. In our work, we focus only on the effect of the exfoliation process and how it can affect the photocatalytic properties. The present study investigates how the graphite type used in synthesizing graphene oxide (GO) affects the exfoliation of sheets and its photocatalytic properties, which is crucial for optimizing hydrogen production efficiency when GO is used as a catalyst. Previous research indicates that graphite characteristics—such as mesh size, degree of oxidation, and number of layers—directly influence the amount of functional oxygen in GO and, consequently, its ability to produce hydrogen under UV irradiation. The insights gained from this study are vital for designing next generation photocatalysts, as they will enable the fine-tuning of synthesis parameters to achieve desired properties. This work evaluates the impact of four graphite sources, all subjected to the same synthesis methodology (patent registered number: MX-a2018-014101).

## 2. Materials and methods

### 2.1. Graphene oxide synthesis

Chemical graphene oxide (GO) synthesis reagents were purchased from Sigma-Aldrich, St. Louis, MO, USA. The synthesis of GO utilized 4 different mineral graphite as the raw material. The main difference between these graphites was the mesh size, which was classified according to ASTM E-11-22 and labeled as Graphite 1 (Taylor 200 mesh), Graphite 2 and 3 (Taylor 325 mesh), and Graphite 4 (Taylor 28 mesh). The graphite samples with varying mesh sizes were oxidized using the same parameters (temperature, time, acid concentration) by the modified Hummers method, as previously reported [17]:

- i) To facilitate ion intercalation, a 3:1 mixture of concentrated  $\text{H}_2\text{SO}_4/\text{HNO}_3$  was added to the graphite (Gr).
- ii) Graphite was oxidized to obtain graphite oxide (GrO) by diffusing  $\text{KMnO}_4$  in an exothermic reaction at approximately 40 °C. Subsequently, the GrO was heated to 85 °C and stirred for 24 h.
- iii) Water and  $\text{H}_2\text{O}_2$  were used to complete the exothermic reaction and facilitate the exfoliation of the material.
- iv) After the stop reaction with  $\text{H}_2\text{O}_2$ , the obtained solution was washed several times with water until pH 7.

### 2.2. Chemical, optical, and structural characterization

Structural analysis of graphite and the resulting graphene oxide (GO) from each pristine graphite was performed using a Panalytical Empyrean diffractometer. X-ray diffraction (XRD) was conducted with  $\text{Cu K}\alpha$  radiation (1.5406 Å) at 45 kV and 40 mA. The crystallite size and interlaminar distance were determined from the (002) reflection of the pristine graphite. These parameters were obtained from the (001) reflection for the GO samples, recorded at 0.01° steps with an interval of 80 s per step. The Scherrer equation and Bragg's law were used to calculate the crystallite size and interlaminar distance, respectively [18]. Finally, the number of layers was calculated by Eq. (1) [19]:

$$N_{hkl} = \frac{L_{hkl}}{d_{hkl}} \quad (1)$$

$N_{hkl}$  is the number of layers,  $L_{hkl}$  is the crystallite size, and  $d_{hkl}$  is the interlaminar distance. In addition, both pristine graphite and GO samples were characterized using scanning electron microscopy (SEM) with a Philips XL30 ESEM system. SEM observations were used to determine the lateral size and distribution of the GO. The sample morphology of the GO was further evaluated using atomic force microscopy (AFM) with an Asylum MFP 3D-SA AFM microscope. A silicon cantilever with rectangular geometry was employed, featuring a length of 160 μm, a constant stiffness of approximately 26 N/m, an average resonance frequency of 300 kHz, and a tip radius of about 9 nm. The GO samples were analyzed after centrifugation and deposition via the “drop-casting” method on a silica grid. The root-mean-square (RMS) roughness was calculated using Eq. (2).

$$RMS = \frac{1}{MN} \sum_{K=0}^{M-1} \sum_{L=0}^{N-1} ((zxk, yl))^2 \quad (2)$$

Optical properties were analyzed using a Shimadzu UV–Vis CARY 100 spectrophotometer. Chemical characterization was performed using Fourier transform infrared spectroscopy (FTIR) and X-ray photoelectron spectroscopy (XPS). For FTIR, samples were measured with a Shimadzu IRTracer-100 spectrophotometer in the 500–4000 cm<sup>-1</sup> range respectively, were used. The thermal stability studies were carried out using thermogravimetric (TGA) equipment and a differential scanning calorimetry analysis of the DCS-SDT model Q600 from TA Instruments. XPS analysis was conducted with a Thermo Scientific Escalab 250Xi spectrometer equipped with a monochromatic Al K $\alpha$  source (1486.68 eV) and an analysis radius of 650 μm. High-resolution spectra for C1s and O1s were obtained with a pass energy of 20 eV, a take-off angle of 45°, and a step size of 0.1 eV. The O/C ratio was calculated following procedures reported in the literature [20], which involved analyzing the areas of the O1s and C1s peaks and their respective relative sensitivity factors (RSF).

### 2.3. Photocatalytic characterization

The photocatalytic properties of the obtained graphene oxide (GO) were evaluated for hydrogen production under UV light irradiation. In a typical experiment, 5 mg of GO was added to 150 mL of a 1:1 volume ratio water/methanol solution in a Pyrex reactor, with methanol acting as a scavenger [21]. A mercury pen lamp (254 nm, 4.4 mW/cm<sup>2</sup>), housed in a quartz tube and immersed in the solution, served as the light source. Hydrogen production was measured hourly using a GOW-MAC Series 580 chromatograph with a thermal conductivity detector (TCD). The kinetic rate constant  $K$  was calculated using the integral method for an irreversible monomolecular reaction of zero order [22]:

$$r_A = \frac{dC_A}{dt} = K \quad (3)$$

where  $C_A$  is the hydrogen concentration at time  $t$ .

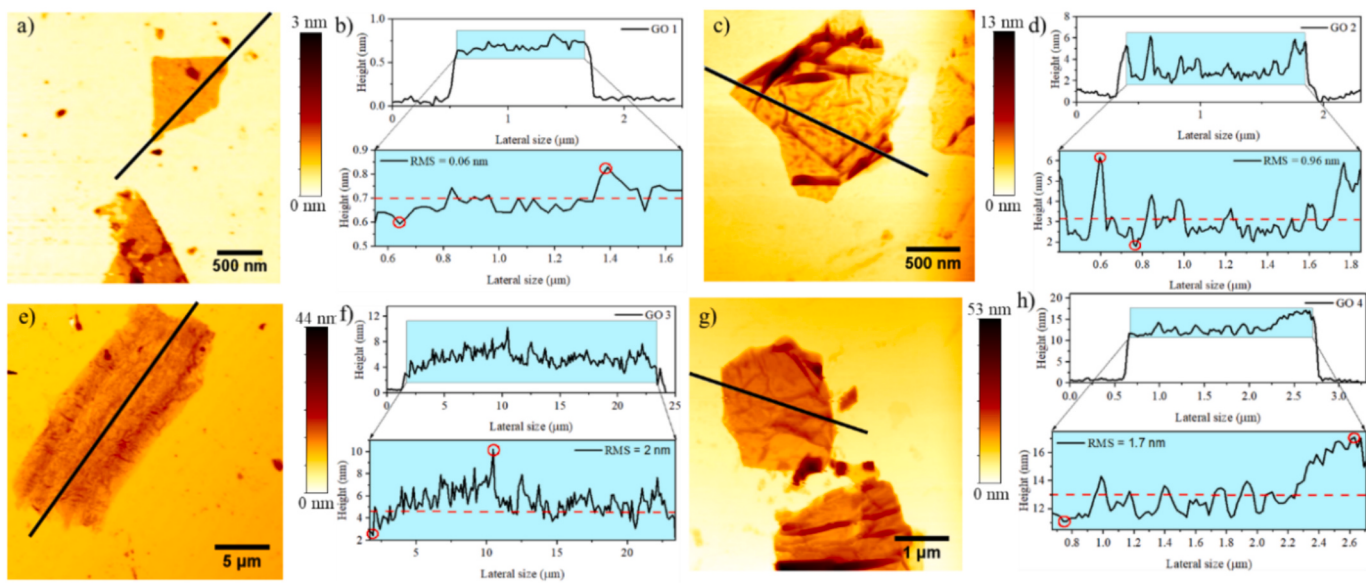


**Fig. 1.** AFM image, Height, and Roughness profile: GO1 a–b, GO2 c–d, GO3 e–f, and GO4 g–h, respectively.

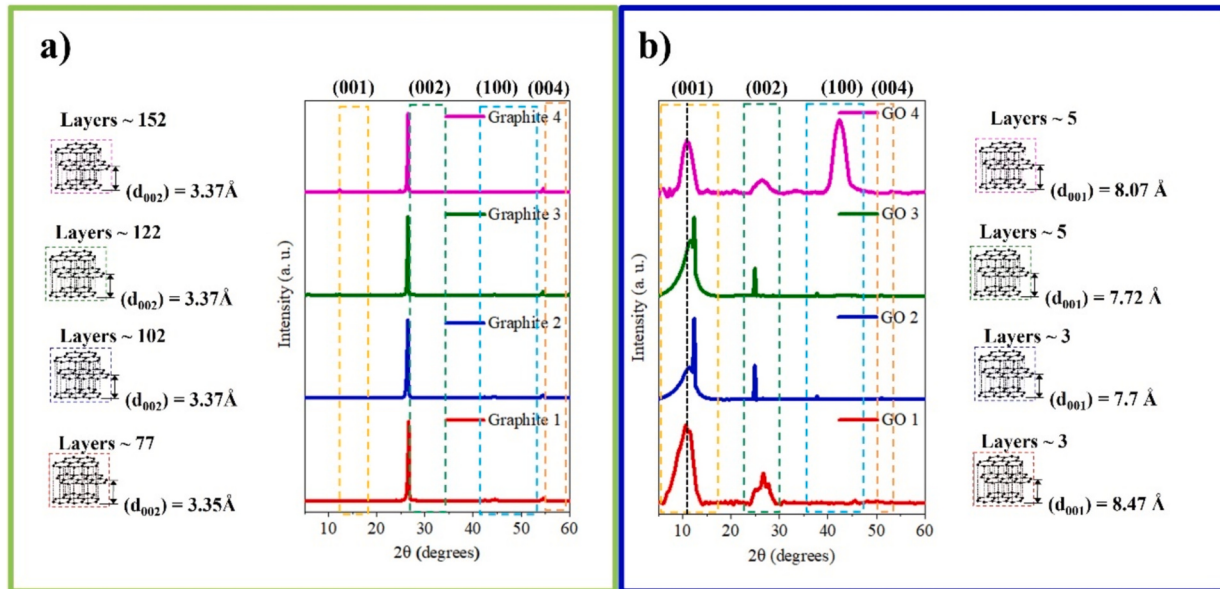


**Fig. 2.** Diffractograms from pristine a) Graphite 1–4 and Graphene Oxides b) GO 1–4.

### 3. Results and discussion

#### 3.1. Number of layers analysis

Fig. 1a presents a micrograph of GO1 with a black line over it, where the dark colors correlated with the lateral bar highlight characteristic

**Table 1**

Layer-to-layer distance of different graphite samples before and after the oxidation and exfoliation processes.

Raw material	GO				
	Sample	d <sub>hkl</sub> (Å)	# Layers	Layer-layer distance (Å)	# Layers
Graphite 1	3.37	77	8.47	3	
Graphite 2	3.37	102	7.7	3	
Graphite 3	3.37	122	7.72	5	
Graphite 4	3.37	152	8.07	5	

wrinkles and folds [2]. Fig. 1b shows the corresponding height profile of GO1, which reveals a thickness of approximately 0.7 nm and a root-mean-square (RMS) roughness value of 0.06 nm. Similarly, Fig. 1c displays a micrograph of GO2 with a black profile section that highlights wrinkles on the surface and folds or stacked layers at the edges. The height profile in Fig. 1d shows that GO2 has a greater thickness of about 3.1 nm, with an RMS roughness value of 0.96 nm. Fig. 1e provides a micrograph of GO3, with a black profile section illustrating a rough surface, as indicated by the color scale. The height profile in Fig. 1f shows that GO3 has a thickness of around 4.4 nm and an RMS roughness value of 2 nm. Finally, Fig. 1g shows a micrograph of GO4 with a black profile section that highlights pronounced folds and wrinkles. Fig. 1h presents the corresponding height profile, indicating that GO4 has a thickness of approximately 13 nm and an RMS roughness value of 1.7 nm.

Fig. 2a shows the XRD diffractograms of different pristine graphite samples. All diffractograms exhibit two distinct peaks at 26.5° and

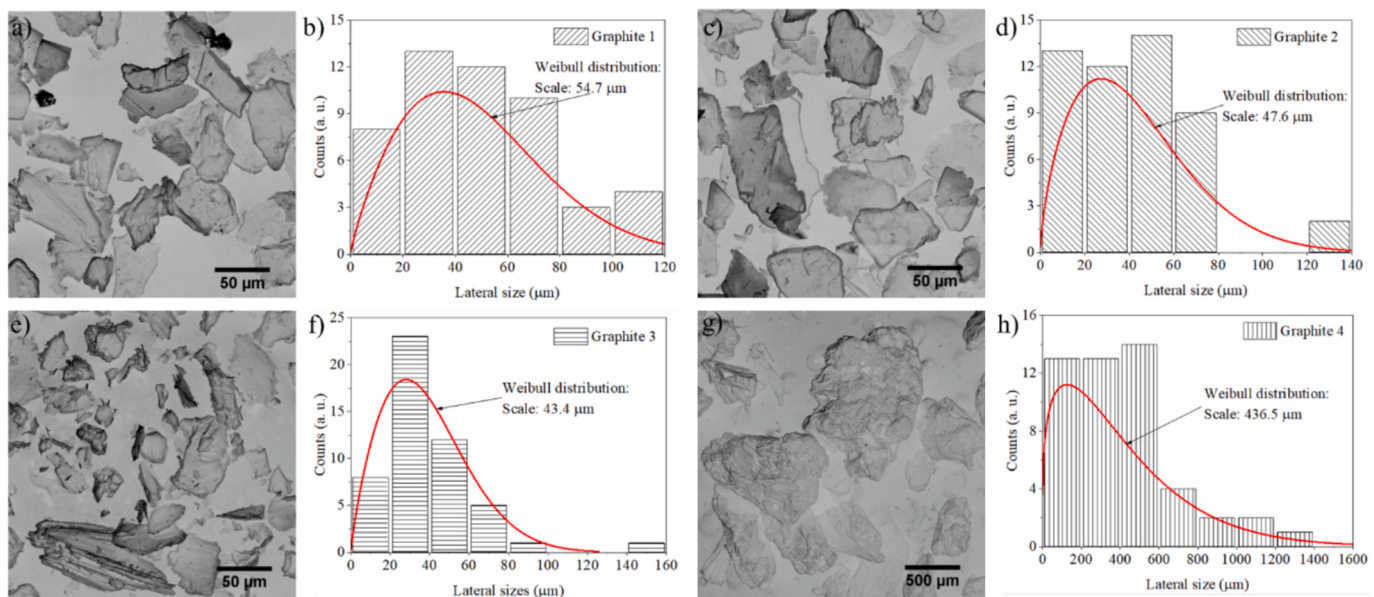


**Fig. 3.** SEM micrographs and lateral size Weibull distribution: Graphite 1 a–b, 2 c–d, 3 e–f, and 4 g–h, respectively.

54.6°, corresponding to the (002) and (004) planes, respectively. Using the Bragg equation [23], the interlayer distance between adjacent graphitic layers was calculated from the reflection at  $2\theta = 26.5^\circ$ , yielding an interlayer distance  $d_{hkl}$  of approximately 3.37 Å.

The number of stacked graphite layers was calculated using the Scherrer equation [24], resulting in values of 254.7 Å, 339.8 Å, 407.6 Å, and 509.5 Å for Graphite 1, 2, 3, and 4, respectively (see Table 1). These values correspond to approximately 77 stacked layers for Graphite 1, about 102 for Graphite 2, 122 for Graphite 3, and 152 for Graphite 4. After the oxidation and exfoliation processes, an increase in the full width at half maximum (FWHM) of the (002) plane was observed. This increase indicates a loss of crystallinity due to layer separation and the amorphization of graphite.

For sample GO1, a peak at 10.4° corresponding to the (001) plane confirmed the exfoliation of Graphite 1 (see Fig. 1b). A lower intensity peak at 26.6°, corresponding to the (002) plane, was also observed, along with a third low-intensity peak at 45.6°, related to the (100) plane.

**Table 1** summarizes the diffraction peaks for all GO sheets obtained from the oxidation and exfoliation processes.

The shift in the diffraction peaks of the (002) and (100) planes is attributed to the incorporation of exfoliated material and oxygen functional groups between layers [25]. Using the angle of reflection for the (001) plane in the Bragg equation [21], the average distance between adjacent layers of the graphene oxide (GO) was calculated. The results showed an interlayer distance of 8.47 Å for GO1, 7.7 Å for GO2, 7.72 Å for GO3, and 8.07 Å for GO4. Additionally, the Scherrer equation [22] was used to determine the average height of the stacked materials. The height of GO1 was calculated to be 21.51 Å, and GO2 had a height of approximately 24.85 Å, corresponding to roughly  $3 \pm 1$  stacked layer in both cases. In comparison, GO3 had a height of about 27.1 Å, and GO4 had a height of approximately 2.96 Å, indicating of  $5 \pm 1$  stacked layer for GO3 and GO4. The number of layers in the GO samples was also assessed from height profiles obtained via AFM.

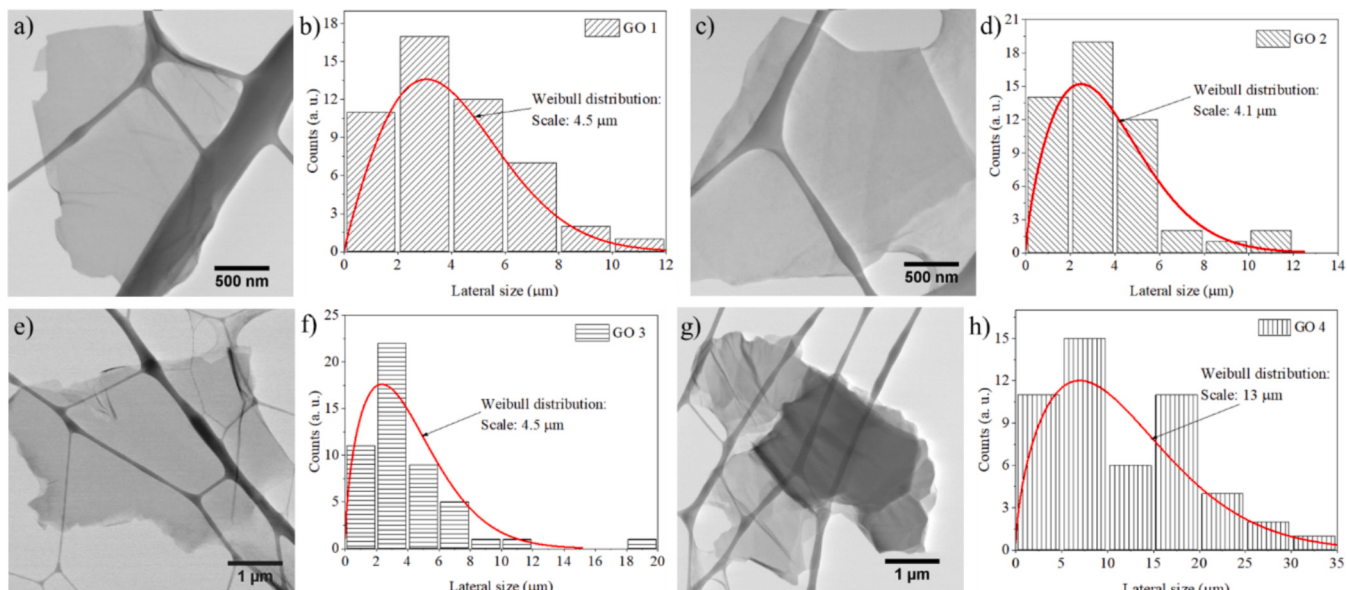


**Fig. 4.** SEM-STEM image and lateral size Weibull distribution: GO1 a–b, GO2 c–d, GO3 e–f, and g) GO4 g–h, respectively.

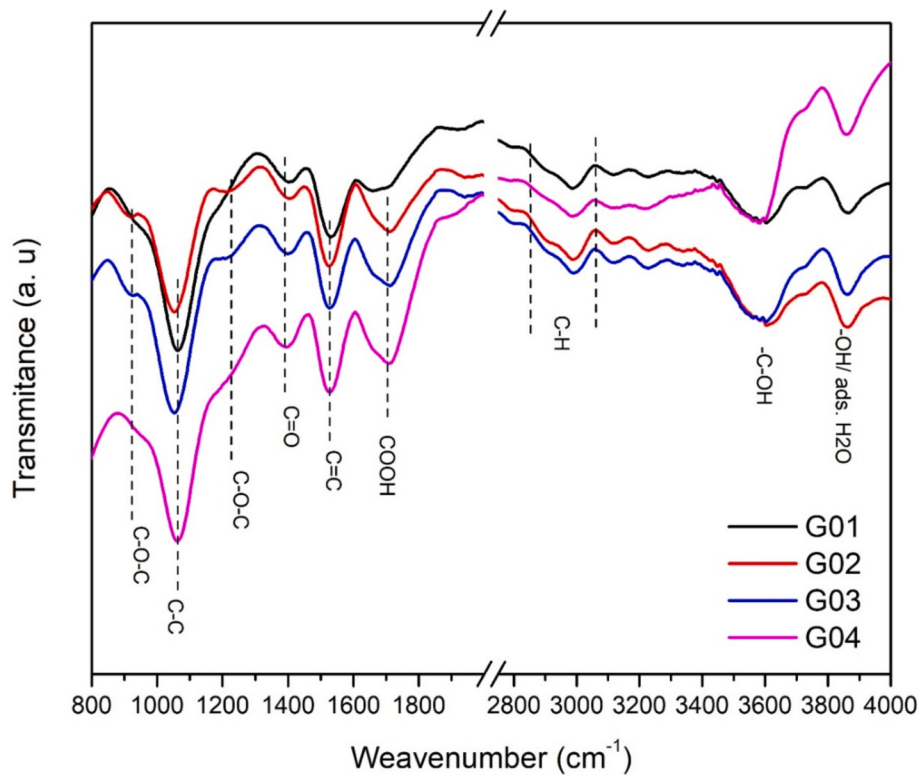


**Fig. 5.** FTIR spectra of the different graphene oxide (GO) samples obtained.

### 3.2. Structural analysis

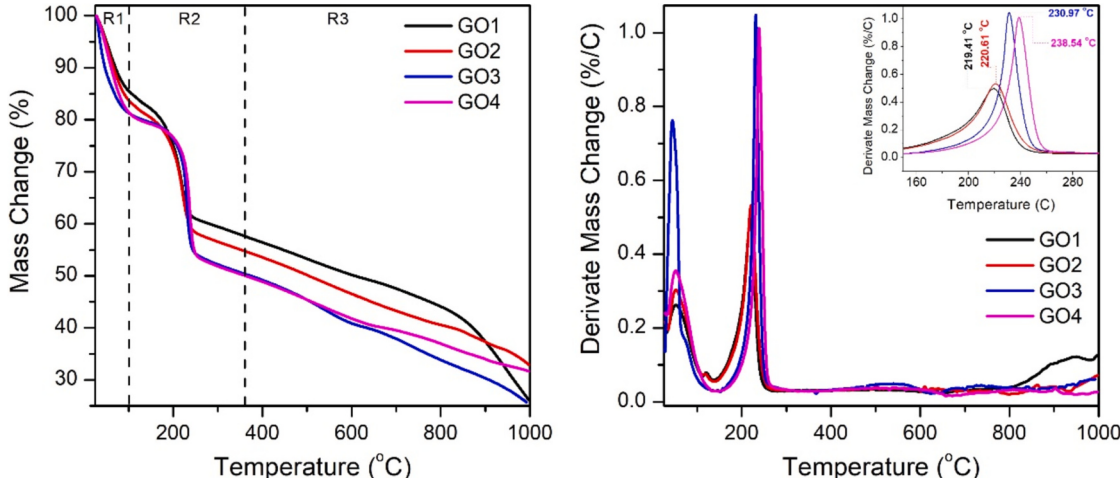
Fig. 3a shows a representative micrograph of Graphite 1, which displays a range of sizes with a lateral size following a Weibull distribution of 54.7  $\mu\text{m}$  (Fig. 3b). Graphite 2, depicted in Fig. 3c, exhibits minor variations in lateral size, with a Weibull distribution of approximately 47.6  $\mu\text{m}$ . Fig. 3e shows a representative micrograph of Graphite 3, which has a wide size variation and a lateral size of about 43.4  $\mu\text{m}$ , as illustrated in Fig. 3f. Finally, Fig. 3g presents a micrograph of Graphite 4, which features larger sizes than the other graphites with a Weibull distribution of approximately 436.5  $\mu\text{m}$ .

Fig. 4 shows the micrographs of graphene oxide (GO) sheets obtained through different processes. Fig. 4a displays a representative micrograph of GO1, which has few wrinkles and a lateral size of around 3  $\mu\text{m}$ . The lateral size Weibull distribution for GO1 has a scale of 4.5  $\mu\text{m}$

compared to the literature [26]. Fig. 4c presents GO2, which features an almost flattened surface with a lateral size of approximately 2  $\mu\text{m}$ . The Weibull distribution for GO2 has a scale of about 4.1  $\mu\text{m}$ . Fig. 4e shows GO3 with several folds at the edges and a lateral size of around 3  $\mu\text{m}$ . The Weibull distribution for GO3 has a scale of approximately 4.5  $\mu\text{m}$ , as depicted in Fig. 4f. Fig. 4g illustrates GO4, which has about 5 stacked layers, indicated by the changes between transparent and nearly opaque surfaces as reported in the literature [27]. GO4 also exhibits some wrinkles and a lateral size of around 4  $\mu\text{m}$ , with a Weibull distribution scale of 13  $\mu\text{m}$ .

### 3.3. Chemical analysis

Fourier transform infrared (FTIR) analysis was used to determine the chemical structural changes between the GO samples, as shown in Fig. 5.



**Fig. 6.** (a) TGA and (b) DTG thermograms of the GO's samples.

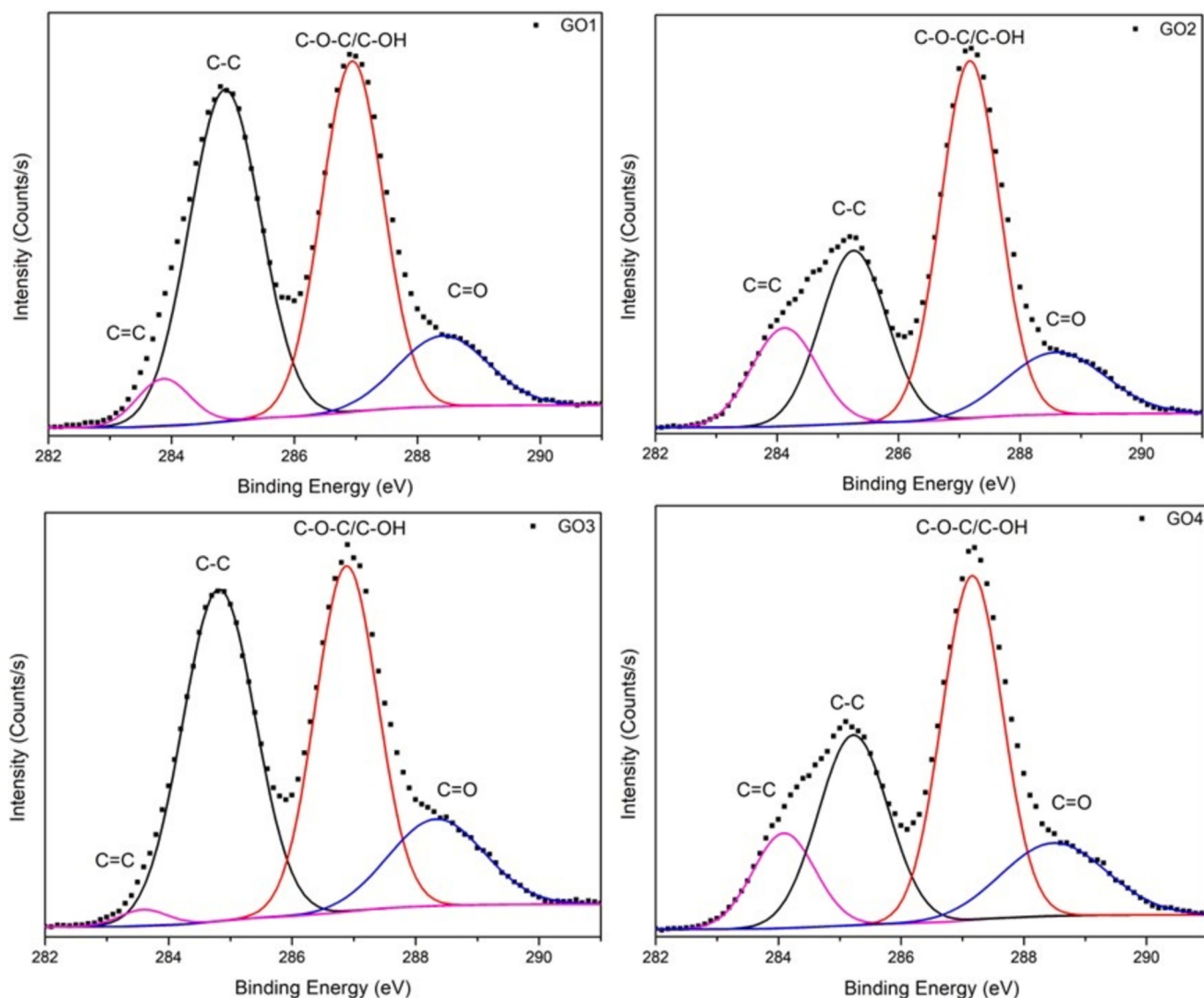


Fig. 7. XPS spectra of the C1s region for the different GO samples.

All samples exhibit characteristic peaks for the skeletal modes of C—C [28] and C=C [29–31] stretching in aromatic rings at  $1065\text{ cm}^{-1}$  and  $1530\text{ cm}^{-1}$ , respectively. Each spectrum displays several bands associated with oxygen-containing functional groups, including the symmetric stretching of the C=O group at  $1390\text{ cm}^{-1}$  [32]. A broadband between  $3100$  and  $3700\text{ cm}^{-1}$  attributed to hydroxyl groups (-C-OH) [28,33]. The -OH group and adsorbed H<sub>2</sub>O at  $3860\text{ cm}^{-1}$  [29]. Additionally, all samples show a broad band between  $3020$  and  $2850\text{ cm}^{-1}$  due to C—H stretching. The peaks at  $3020$  and  $2940\text{ cm}^{-1}$  correspond to  $\text{sp}^2$  C—H stretching, while the peak at  $2850\text{ cm}^{-1}$  is due to  $\text{sp}^3$  C—H stretching [34]. The key differences among the samples are observed in the  $900$  and  $1240\text{ cm}^{-1}$  signals. These signals are visible in GO2 and GO3

**Table 2**

Mass reduction of different graphene oxide (GO) samples across three temperature regions:

Temperature (°C)	Mass change (%)			
	GO1	GO2	GO3	GO4
25–100	85.55	83.75	81.32	81.46
100–360	57.64	54.77	50.37	50.06
360–1000	26.69	33.25	25.70	31.80

but less noticeable in GO1 and GO4. These peaks correspond to the vibrational modes of epoxides (C-O-C) [33].

Fig. 6 shows the GO samples' thermogravimetric (TGA) and derivative thermogravimetric (DTG) analyses. The analyses reveal three distinct temperature regions with characteristic mass loss steps for all samples: R1 (25–100 °C): Associated with water evaporation. R2 (100–360 °C): Related to the decomposition of oxygen-containing groups. R3 (360–1000 °C): Linked to the oxidative pyrolysis of the carbon framework [35,36].

As indicated in the table, samples GO3 and GO4 exhibit a more significant mass reduction than GO1 and GO2, suggesting a higher content of oxygen-containing groups. Additionally, GO4 shows a smaller mass decrease in the 360–1000 °C range, indicating either a higher number of layers in the material or high stability of the carbon framework.

All samples exhibited two DTG peaks corresponding to the R1 and R2 regions. The  $T_{\max}$  of the peaks in the R2 region represents the maximum thermal energy required to break the bonds of oxygen species attached to the carbon atoms in the different GO samples [35].  $T_{\max}$  values in the R2 region were found to be 219.41 °C, 220.61 °C, 230.97 °C, and 238.54 °C for samples GO1, GO2, GO3, and GO4, respectively. Higher  $T_{\max}$  values suggest greater stability of the oxygen species, with the

**Table 3**

Binding energies, the percentage content of assigned species in the C1s region, and O/C ratios for the GO samples.

Sample	C=C (283.9 ± 0.25 eV)	C-C (285.0 ± 0.23 eV)	C-O-C/C-OH (287.0 ± 0.15 eV)	C=O (288.4 ± 0.11 eV)	O/C ratio
GO1	4.64 %	43.74 %	39.94 %	11.66 %	0.47
GO2	14.39 %	25.36 %	46.63 %	13.60 %	0.50
GO3	1.46 %	44.09 %	39.38 %	15.04 %	0.55
GO4	12.43 %	27.90 %	43.70 %	15.96 %	0.52

stability increasing in the following order: GO1 < GO2 < GO3 < GO4.

Fig. 7a-d displays the XPS C1s spectra of the GO samples. Each spectrum shows two main characteristic peaks of graphene oxide: around 284.8 eV and 286.5 eV. These peaks correspond to carbon atoms bonded to other carbons and carbon atoms bonded to oxygen. The C1s signal was deconvoluted into four components:  $sp^2$  C=C bond at 283.9 eV,  $sp^3$  C—C bond at 285 eV, C-O-C/C-OH bonds at 287 eV, and C=O bond at 288.4 eV. These components are detailed in Table 2.

The percentages of C—C species vary among the samples, with the lowest amounts observed in GO2 and GO4 and the highest in GO1 and GO3. Conversely, the amount of C-O-C/C-OH bonds increases in samples with lower C—C content, and the C=O bond content increases from GO1 to GO4 (as shown in Table 3). The GO samples' oxygen-to-carbon (O/C) ratio ranges from 0.47 to 0.55, indicating varying degrees of oxidation among the materials. The amount of oxygen-containing functional groups in the materials is related to the number of active sites available. The analysis of the C1s region indicates that all samples possess a substantial number of oxygen functional groups, suggesting a high capacity for anchoring metal ions or adsorbing organic molecules [37–39].

#### 3.4. Photocatalytic hydrogen production

All GO materials exhibit photocatalytic activity for hydrogen production under UV irradiation, as shown in Fig. 8. This indicates that all samples can serve as adequate photocatalytic supports. Among the

samples, GO4 demonstrated the highest hydrogen production, reaching 1570  $\mu\text{mol/g}$  over 4 h, whereas GO1 showed the lowest activity with 1335  $\mu\text{mol/g}$ . The trend in hydrogen production correlates with the O/C ratio, as determined by XPS, suggesting that higher hydrogen production is associated with a higher O/C ratio, primarily due to the presence of the C=O bond.

Fig. 7 includes the kinetic constants for the materials, where GO1 exhibited the highest kinetic constant at 305  $\mu\text{mol/h}$ , followed by GO2 at 302  $\mu\text{mol/h}$ , GO3 at 285  $\mu\text{mol/h}$ , and GO4 at 258  $\mu\text{mol/h}$ .

Analyzing Fig. 8 reveals that while the GO4 sample shows the highest photocatalytic hydrogen production over 4 h, the relative advantage of GO4 over the other samples decreases progressively. Initially, GO4's hydrogen production was 47 %, 40 %, and 24 % higher than GO1, GO2, and GO3, respectively. By the fourth hour, the production differences had narrowed to 15 %, 12 %, and 9 % compared to GO1, GO2, and GO3, respectively. This behavior could be explained by the loss of C-OH, C-O-C, and possibly C=O groups due to prolonged UV irradiation during the experiments, as reported by other studies [40].

As demonstrated in this study, advancements in synthesizing graphene oxide (GO) based materials hold significant potential for clean energy applications, including lithium-ion batteries, solar cells, supercapacitors, and hydrogen production. Notably, the observation that GO synthesized from graphite with smaller mesh sizes shows higher hydrogen production, which suggests that the GO synthesis process can be optimized for specific applications. The study reveals that functional groups, such as the increased C=O groups in materials with superior photocatalytic performance, provide valuable insights for designing efficient hydrogen production materials and extend to other areas of photocatalysis. This work enhances the current understanding of how different graphite sources influence GO properties and sets the stage for future developments in renewable energy and photocatalysis technologies. Consequently, GO emerges as a highly versatile and promising material for addressing global energy challenges.

#### 4. Conclusions

According to our study, the lateral size and number of layers of

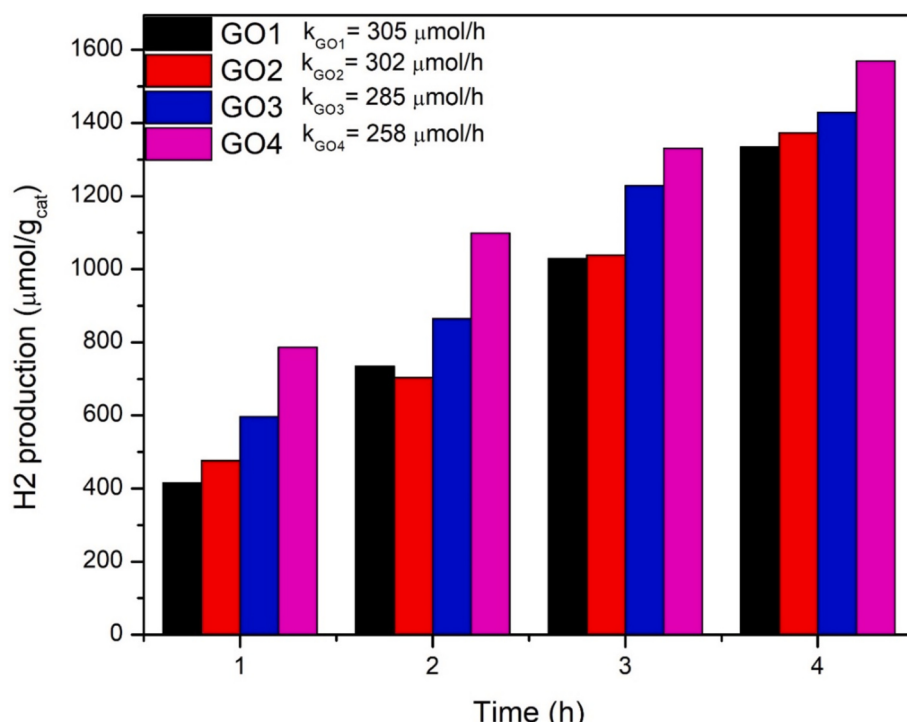


Fig. 8. Photocatalytic H<sub>2</sub> production under UV light irradiation in all GO samples.

pristine graphite significantly influence the lateral size distribution, oxidation degree, content of functional oxygen groups, and photocatalytic properties of graphene oxide (GO). AFM analysis revealed that the roughness of the GO samples was 0.7 nm for GO1, 3.1 nm for GO2, 2 nm for GO3, and 14 nm for GO4. XRD measurements indicated that all oxidized materials exhibited stacking between 3 and 5 layers. SEM-STEM images showed a similar lateral size of approximately 4.5  $\mu\text{m}$  for GO1, GO2, and GO3, whereas GO4 exhibited a larger size of up to 13  $\mu\text{m}$ .

FTIR and XPS analyses identified various functional groups in the samples, with GO4 showing higher C=O groups than the other samples. TGA results indicated high stability for GO4, likely due to its larger size and higher content of oxygen functional groups. In photocatalytic evaluations, GO4 demonstrated the highest hydrogen production over 4 h. Therefore, this work highlights the significant impact of UV radiation exposure time on H<sub>2</sub> production from GO samples, demonstrating a reduction of up to 32 % in hydrogen production.

#### CRediT authorship contribution statement

**E.A. Huitrón-Segovia:** Writing – original draft, Methodology, Data curation. **D. Torres-Torres:** Writing – review & editing, Supervision, Data curation, Formal Analysis. **A. Moreno-Bárcenas:** Writing – review & editing, Visualization, Data curation. **J.E. Samaniego-Benítez:** Writing – review & editing, Validation, Formal analysis, Data curation. **J. Ramírez-Aparicio:** Writing – review & editing, Formal analysis. **A. Mantilla:** Writing – review & editing, Resources. **A. García-García:** Writing – review & editing, Supervision, Methodology, Investigation, Funding acquisition, Formal analysis, Conceptualization.

#### Declaration of competing interest

The authors declare that they have no known competing financial interests or personal relationships that could have appeared to influence the work reported in this paper.

#### Acknowledgments

The authors thank Nayely Pineda Aguilar, Luis Gerardo Silva, Alonso Concha Valderrama, Oscar E. Vega, and Lilia Magdalena Bautista Carrillo at Centro de Investigación en Materiales Avanzados S.C. for infrastructure and technical support.

#### Data availability

No data was used for the research described in the article.

#### References

- [1] R. Raccichini, A. Varzi, S. Passerini, B. Scrosati, The role of graphene for electrochemical energy storage, *Nat. Mater.* 14 (3) (2015) 271–279, <https://doi.org/10.1038/nmat4170>.
- [2] A.S. Nimbalkar, S.K. Tiwari, S.K. Ha, C.K. Hong, An efficient water saving step during the production of graphene oxide via chemical exfoliation of graphite, *Mater. Today Proc.* 21 (2020) 1749–1754, <https://doi.org/10.1016/j.mtpr.2020.01.227>.
- [3] A.F. Faria, F. Perreault, M. Elimelech, Elucidating the role of oxidative debris in the antimicrobial properties of graphene oxide, *ACS Appl Nano Mater* 1 (2018) 1164–1174, <https://doi.org/10.1021/acsnano.7b00332>.
- [4] A.F. Betancur-Lopera, et al., Role of low-dimensional carbon nanostructures in hybrid material as anticorrosive coating, *Prog. Org. Coat.* 163 (December 2021) (2022), <https://doi.org/10.1016/j.porgcoat.2021.106682>.
- [5] S. Gurunathan, J.W. Han, A.A. Dayem, V. Eppakayala, J. Kim, Oxidative stress-mediated antibacterial activity of graphene oxide and reduced graphene oxide in *Pseudomonas aeruginosa*, *Int. J. Nanomedicine* 7 (2012) 5901–5914.
- [6] X. Zeng, B.-B. Zhu, W. Qiu, W.-L. Li, X. Zheng, B. Xu, A review of the preparation and applications of wrinkled graphene oxide, *New Carbon Materials* 37 (2) (2022) 290–302.
- [7] W.S. Hummers Jr., R.E. Offeman, Preparation of graphitic oxide, *J. Am. química Soc.* 80 (6) (1958) 1339, <https://doi.org/10.1021/ja01539a017>.
- [8] S. Shamaila, A.K.L. Sajjad, I. Anum, Modifications in development of graphene oxide synthetic routes, *Chem. Eng. J.* (2016), <https://doi.org/10.1016/j.cej.2016.02.109> (no. February).
- [9] B.E. Rodríguez, et al., Influence of multidimensional graphene oxide (GO) sheets on anti-biofouling and desalination performance of thin-film composite membranes: effects of GO lateral sizes and oxidation degree, *Polymers (Basel)* 12 (12) (2020) 1–24, <https://doi.org/10.3390/polym12122860>.
- [10] A. Moreno-Bárcenas, J.F. Perez-Robles, Y.V. Vorobiev, I.E. Pech-Pech, A.G. García, Facile in-situ reduction method for preparation of GO-Pd catalysts, *Int. J. Electrochem. Sci.* 13 (3) (2018) 3171–3184, <https://doi.org/10.20964/2018.03.31>.
- [11] E. Mahmoudi, W.L. Ang, C.Y. Ng, L.Y. Ng, A.W. Mohammad, A. Benamor, Distinguishing characteristics and usability of graphene oxide based on different sources of graphite feedstock, *J. Colloid Interface Sci.* 542 (2019) 429–440, <https://doi.org/10.1016/j.jcis.2019.02.023>.
- [12] C. Botas, et al., The effect of the parent graphite on the structure of graphene oxide, *Carbon N Y* 50 (1) (2012) 275–282, <https://doi.org/10.1016/j.carbon.2011.08.045>.
- [13] Z. Wu, W. Ren, L. Gao, B. Liu, C. Jiang, H. Cheng, Synthesis of high-quality graphene with a pre-determined number of layers, *Carbon N Y* 47 (2) (2008) 493–499, <https://doi.org/10.1016/j.carbon.2008.10.031>.
- [14] M. Sieradzka, C. Ślusarczyk, R. Fryczkowski, J. Janicki, Insight into the effect of graphite grain sizes on the morphology, structure and electrical properties of reduced graphene oxide, *J. Mater. Res. Technol.* 9 (4) (2020) 7059–7067, <https://doi.org/10.1016/j.jmrt.2020.05.026>.
- [15] Y. Xia, L. Zhang, J. Yu, Graphene oxide-based photocatalysts for H<sub>2</sub> production, in: *Graphene Oxide-Metal Oxide and Other Graphene Oxide-Based Composites in Photocatalysis and Electrocatalysis*, 2022, <https://doi.org/10.1016/B978-0-12-842526-2.00003-9>.
- [16] H. Khan, Graphene based semiconductor oxide photocatalysts for photocatalytic hydrogen (H<sub>2</sub>) production, a review, *Int. J. Hydrogen Energy* 84 (2024) 356–371, <https://doi.org/10.1016/j.ijhydene.2024.08.057>.
- [17] E. Alejandra Huitrón Segovia, D. Torres-Torres, J. Raúl Pérez Higareda, A. García-García, Indentation size effects in graphene oxide under suspended nanoindentation, *Mech. Mater.* 158 (2021) 103875, <https://doi.org/10.1016/j.mechmat.2021.103875>.
- [18] A. Kaushal, S.K. Dhawan, V. Singh, Determination of crystallite size, number of graphene layers and defect density of graphene oxide (GO) and reduced graphene oxide (RGO), *AIP Conf. Proc.* 2115 (1) (Jul. 2019) 030106, <https://doi.org/10.1063/1.5112945>.
- [19] S. Hun, Thermal reduction of graphene oxide, *Physics and Applications of Graphene: Experiments* 19 (2011) 73–90.
- [20] A. Kovtun, D. Jones, S. Dell'Elce, E. Treossi, A. Liscio, V. Palermo, Accurate chemical analysis of oxygenated graphene-based materials using X-ray photoelectron spectroscopy, *Carbon N Y* 143 (2019) 268–275, <https://doi.org/10.1016/j.carbon.2018.11.012>.
- [21] F. Guzman, S.S.C. Chuang, C. Yang, Role of methanol sacrificing reagent in the photocatalytic evolution of hydrogen, *Ind. Eng. Chem. Res.* 52 (1) (Jan. 2013) 61–65, <https://doi.org/10.1021/ie301177s>.
- [22] F. Galindo-Hernández, et al., On the role of Fe<sup>3+</sup> ions in Fe<sub>x</sub>O<sub>y</sub>/C catalysts for hydrogen production from the photodehydrogenation of ethanol, *J. Hazard. Mater.* 263 (Dec. 2013) 11–19, <https://doi.org/10.1016/j.jhazmat.2013.08.015>.
- [23] N.I. Zaaba, K.L. Foo, U. Hashim, S.J. Tan, W.W. Liu, C.H. Voon, Synthesis of graphene oxide using modified hummers method: solvent influence, in: *Procedia Engineering*, Elsevier Ltd, 2017, pp. 469–477, <https://doi.org/10.1016/j.proeng.2017.04.118>.
- [24] U. Holzwarth, N. Gibson, The Scherrer equation versus the 'Debye-Scherrer equation', *Nat. Nanotechnol.* 6 (9) (2011) 534.
- [25] R.D. Martínez-Orozco, H.C. Rosu, S.-W. Lee, V. Rodríguez-González, Understanding the adsorptive and photoactivity properties of Ag-graphene oxide nanocomposites, *J. Hazard. Mater.* 263 (2013) 52–60.
- [26] Y. Liao, Z. Li, W. Xia, Size-dependent structural behaviors of crumpled graphene sheets, *Carbon N Y* 174 (2021) 148–157.
- [27] J. Guerrero-Contreras, F. Caballero-Briones, Graphene oxide powders with different oxidation degree, prepared by synthesis variations of the Hummers method, *Mater. Chem. Phys.* 153 (Mar. 2015) 209–220, <https://doi.org/10.1016/j.matchemphys.2015.01.005>.
- [28] T. Szabó, et al., Evolution of surface functional groups in a series of progressively oxidized graphite oxides, *Chem. Mater.* 18 (11) (2006) 2740–2749.
- [29] C. Zhang, D.M. Dabbs, L.-M. Liu, I.A. Aksay, R. Car, A. Selloni, Combined effects of functional groups, lattice defects, and edges in the infrared spectra of graphene oxide, *J. Phys. Chem. C* 119 (32) (2015) 18167–18176.
- [30] S.N. Chanu, P. Sushma, B.S. Swain, B.P. Swain, Optical, chemical bonding and electrochemical properties of vanadium pentoxide/reduced graphene oxide nanocomposite for supercapacitor electrode material, *J. Mater. Sci. Mater. Electron.* 33 (26) (2022) 20487–20497.
- [31] N. Kumar, S. Das, C. Bernhard, G.D. Varma, Effect of graphene oxide doping on superconducting properties of bulk MgB [Online]. Available: <http://doc.rero.ch>.
- [32] S. Singh, et al., Sustainable removal of Cr (VI) using graphene oxide-zinc oxide nanohybrid: adsorption kinetics, isotherms and thermodynamics, *Environ. Res.* 203 (2022) 111891.
- [33] X. He, S. Zhang, H. Pan, J. Chen, J. Xu, Horizontally aggregation of monolayer reduced graphene oxide under deep UV irradiation in solution, *Nanoscale Res. Lett.* 14 (2019) 1–9.
- [34] F.M.C. Caicedo, et al., Synthesis of graphene oxide from graphite by ball milling, *Diamond Relat. Mater.* 109 (2020) 108064.

- [35] F. Farivar, P.L. Yap, R.U. Karunagaran, D. Losic, Thermogravimetric analysis (TGA) of graphene materials: effect of particle size of graphene, graphene oxide and graphite on thermal parameters, *C* (Basel) 7 (2) (2021) 41.
- [36] M. Wojtoniszak, et al., Synthesis, dispersion, and cytocompatibility of graphene oxide and reduced graphene oxide, *Colloids Surf. B Biointerfaces* 89 (2012) 79–85.
- [37] Y. Kuang, J. Shang, T. Zhu, Photoactivated graphene oxide to enhance photocatalytic reduction of CO<sub>2</sub>, *ACS Appl. Mater. Interfaces* 12 (3) (2019) 3580–3591.
- [38] S. Navalon, A. Dhakshinamoorthy, M. Alvaro, M. Antonietti, H. García, Active sites on graphene-based materials as metal-free catalysts, *Chem. Soc. Rev.* 46 (15) (2017) 4501–4529.
- [39] K.M. Iris, et al., Graphite oxide-and graphene oxide-supported catalysts for microwave-assisted glucose isomerisation in water, *Green Chem.* 21 (16) (2019) 4341–4353.
- [40] W.R. Gallegos-Pérez, et al., Effect of UV radiation on the structure of graphene oxide in water and its impact on cytotoxicity and As (III) adsorption, *Chemosphere* 249 (2020) 126160.